Journal of Electronic Materials (2024) 53:5142–5149
https://doi.org/10.1007/s11664-024-11204-8

28TH INTERNATIONAL CONFERENCE ON NUCLEAR TRACKS AND RADIATION MEASUREMENTS

Conducting Polymer-Based Magnetically Active Nanocomposites for Microwave Shielding Materials

Sumit Kumar[1] · Shraddha Agrawal[1] · Vivek Verma[2] · Pratap Singh[1]

Received: 17 December 2023 / Accepted: 20 May 2024 / Published online: 5 June 2024

Abstract
The aggregation of electromagnetic radiation within the spatial environment leads to the disruption of electronic devices used in commercial and military sectors, potentially causing adverse effects on human well-being. There is a growing need for effective shielding materials to manage electromagnetic interference (EMI) and its related issues. It is widely acknowledged that single-composition materials are insufficient in providing the necessary EMI shielding efficiency. As a result, conducting polymer-based composites have garnered significant attention due to their distinctive characteristics, including their light weight, processability, environmental stability, extended lifespan, durability, reduced corrosiveness, and tunability. In this work, the synthesis of conducting polymer nanocomposites consisting of polypyrrole (PPY) and polyaniline (PANI) with nickel and cobalt ferrite nanoparticles was achieved using emulsion polymerization. The ferrite nanoparticles, on the other hand, were synthesized using the sol–gel technique. The investigation focused on examining the microwave absorption characteristics of the composite material within the frequency range of 8.2–12.4 GHz, often referred to as the X-band. The composites based on PANI exhibited remarkably favourable shielding behaviour, attributed primarily to their increased conductivity, resulting in shielding effectiveness of 36 dB (~99.9%). Conversely, the composites based on PPY achieved shielding effectiveness of 25 dB. It is worth noting that the shielding efficiency of both composites was influenced by the magnetization characteristics of the ferrite nanoparticles. The superior shielding properties of absorption, compared to reflection, make composites very promising materials for several applications, including stealth technology and radar absorption.

Keywords Electromagnetic interference · sol–gel · emulsion polymerization

Introduction

A large proportion of today's cutting-edge technology, including satellite and radio and television broadcasting towers, is powered by what is known as electromagnetic radiation (EMR). These types of devices produce radiation over a broad spectrum of frequencies, which then accumulates in the surrounding environment. With the proliferation of mobile phones and other electronic devices that give off electromagnetic (EM) waves, electromagnetic (EM) radiation pollution is an increasing threat.[1–3] Electromagnetic (EM) waves can disrupt signals, cause electrical equipment to break down, and negatively affect human health.[4,5] Given the inevitability of electromagnetic radiation exposure, various electromagnetic interference (EMI) shielding elements have been developed in an effort to mitigate or eliminate the harm caused by EM wave pollution. Most materials that block EMI work through a combination of reflection, absorption, and repeated reflections. Out of these methods, absorption shielding is the most effective method for removing hazardous electromagnetic radiation from the environment.[6] Increasing the frequency, dimensions, and susceptibility of the shielding barrier enhances the effectiveness of EMR absorption. When developing efficient EM wave absorber materials, two of the most important factors to take into account are impedance matching and EM energy attenuation.[7,8] How successfully electromagnetic waves are reflected and attenuated by the EMI shielding material

✉ Sumit Kumar
sumit.phy@gurugramuniversity.ac.in

[1] Department of Physics, Gurugram University, Gurugram, Haryana 122001, India

[2] Department of Physics, Hindu College, University of Delhi, New Delhi, Delhi 110007, India

depends on a number of factors, including components, structure, relative complex permeability, permittivity, and EM impedance matching.[9] The incident electromagnetic waves are very well absorbed by ferrite-based EMI shielding material, which eliminates the possibility of reflection and transmission, maximizes the efficiency of the shielding, and reduces the amount of secondary electromagnetic pollution.[10] In order to accomplish "efficient shielding", magnetic elements are typically used in the hybrid mixtures as a means of improving impedance matching and adjusting multiple attenuation. Efficient EMI shielding may be achieved with the use of a multi-component composite that has magnetic–dielectric synergy.[11–13]

Given their abundance of raw materials, affordability, significant dispersibility, environmentally friendly nature, non-toxicity, strong anticorrosive qualities, and exceptional electromagnetic properties, spinel ferrites have gained recognition as a potential rival in the field of electromagnetic radiation-absorbing magnetic materials.[14] Spinel ferrites are metal oxides with a spinel structure, denoted by the standard formulation AB_2O_4, where A and B are metallic cations positioned at the tetrahedral (A site) and octahedral (B site) crystallographic sites, respectively.[15] A typical ferrite is MFe_2O_4, where M denotes any of the elements Mn, Fe, Co, Ni, Cu, or Zn. Only 8 of the 64 tetrahedral places and 24 of the 32 octahedral locations in a single ferrite unit cell are engaged by cations. Significant interest has been directed towards spinel ferrite nanoparticles characterized by a high surface-to-volume ratio, elevated mechanical strength, increased diffusivity, and acceptable specific heat, in addition to their high electrical and magnetic properties.[16]

However, their restricted absorption bandwidth, high thickness requirements, and dense nature make single-phase spinel ferrite magnetic materials impractical as an EMI shielding material due to the low impedance matching requirements. To achieve high EM wave absorption, it may be possible to use multiphase hybrid spinel ferrite magnetic materials by integrating additional electrically conductive elements. Better impedance matching is required due to the combination of the high permittivity of conductive material and the low dielectric properties of spinel ferrite magnetic material, yielding an adequate permittivity value.[17] In terms of conductive material enforcement, conducting polymer matrix is another engineered thermally resilient material that is well recognized for its strong insulating capabilities as well as higher mechanical resistance.[18] The aromatic configuration of the polymers is advantageous for enhancing heat resistance and electrical characteristics, particularly when doped with appropriate fillers.[19,20] Polyaniline (PANI) and polypyrrole (PPY) have garnered significant interest because of their straightforward synthetic procedure, remarkable stability, and excellent conductivity, which can be adjusted based on the varying levels of oxidation and protonation.[21]

Taking into account the advantages of both ferrite nanoparticles and conducting polymers, in this study we examined the shielding characteristics of nanocomposites of cobalt ferrite and nickel ferrite with PANI and PPY. The results demonstrated highly enhanced and stable shielding properties. Thus, these materials might find application in precision instruments, stealth equipment, trade defence instruments, TV communication, navigation surveillance, and aircraft electronics.

Materials and Methods

The synthesis method plays an essential part in regulating the dimensions, homogeneity, and surface area of the materials being produced. Researchers use a number of different techniques to synthesize spinel ferrites, such as sol–gel, ultrasonic, solvothermal, microwave assisted, ball milling, solid state reaction, hydrothermal, and co-precipitation approaches.[22,23]

The ferrite nanoparticles were synthesized using the sol–gel process, where the nitrate precursors were initially dissolved in water. Cobalt nitrate [$Co(NO_3)_2{\cdot}6H_2O$], nickel nitrate [$Ni(NO_3)_2{\cdot}6H_2O$], ferric nitrate [$(Fe(NO_3)_3{\cdot}9H_2O$], and citric acid were obtained from Fisher Scientific (India). The $Ni(NO_3)_2{\cdot}6H_2O$/$Co(NO_3)_2{\cdot}6H_2O$) and $Fe(NO_3)_3.9H_2O$ compounds were dissolved individually in deionized water using stoichiometric proportions. Next, the solutions were combined with citric acid, which served as a reducing agent, in a molar ratio equal to that of the total nitrate precursors. The mixture was agitated well. The solution pH was neutralized to 7 by adding an ammonia solution. The solution temperature was then increased from ambient temperature to around 70°C and maintained at that level for a few hours. Subsequently, the solution underwent a transformation into a thick and gelatinous state, resulting in the formation of a delicate foam by an exothermic process.[24] The desiccated precursor was then pulverized into a fine powder. The powder was subjected to calcination at a temperature of 450 °C for 1 h, which led to the development of the ferrite phase.

The conducting polymer composites of ferrite nanoparticles were synthesized by in situ emulsion polymerization of monomers in the presence of ferrite samples. Aniline (An), pyrrole (Py), ammonium peroxydisulfate $(NH_4)_2S_2O_8$ (APS), iron chloride, isopropyl alcohol, and ammonium hydroxide solution, all of analytical purity, were purchased from Merck India. Dodecyl benzene sulfonic acid (DBSA) was acquired from Acros Organics. For the PANI composites, an emulsion solution of aniline and DBSA in the presence of ferrite nanoparticles was polymerized using ammonium peroxydisulfate, $(NH_4)_2S_2O_8$, as oxidant. For the PPY-based composites, an emulsion solution of pyrrole and DBSA in the presence of ferrite nanoparticles was polymerized using iron chloride as

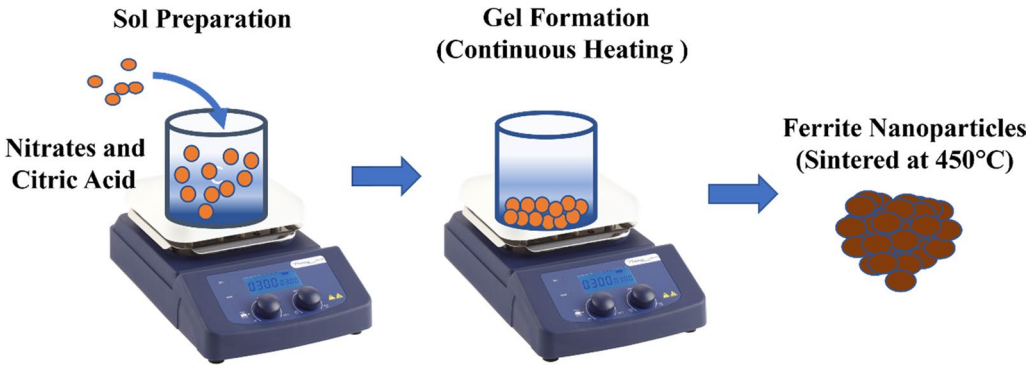

Fig. 1 Synthesis of nanopowders using the sol–gel method with the help of nitrate precursors and citric acid.

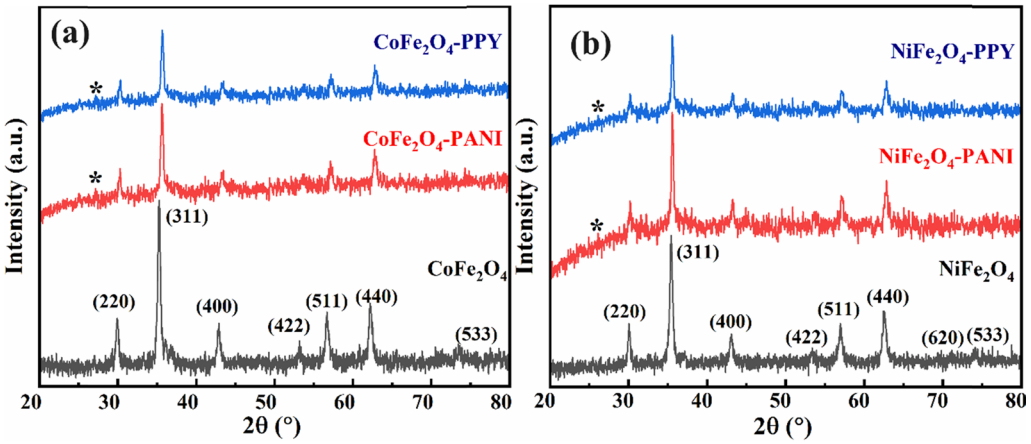

Fig. 2 X-ray diffractograms of ferrite nanoparticles and their composites with PANI and PPY.

oxidant. The reactions were allowed to proceed for 6–8 h at a temperature below 5 °C followed by demulsification and filtration using propanol and water (Fig. 1).

Results and Discussion

Structural Analysis

XRD patterns of nickel and cobalt ferrite samples for their structure and phase purity are shown in Fig. 2 in the 2θ range of 20°–80° (JCPDS card no. 80-0389). The x-ray diffraction (XRD) analysis revealed distinct peaks, confirming the presence of highly crystalline ferrite nanoparticles in a single phase, despite the low sintering temperature of only 450 °C.[25] This can be attributed to the good pH balance and the strong oxidizing effect of citric acid during the sol formation in the sol–gel process.[26] The peaks were indexed as (220), (311), (400), (422), (511), (440), (620), and (533). A single-phase cubic spinel structure having no traces of any additional impurity phases was observed.

Table I Lattice parameters for the ferrite samples computed from diffraction data.

Sample	Lattice constant (Å)	Density (g/cm^3)	Crystallite size (nm)	Hopping length, A site (Å)	Hopping length, B site (Å)
$NiFe_2O_4$	8.4034	5.25	13.4	7.28	5.94
$CoFe_2O_4$	8.4431	5.28	14.2	7.31	5.97

The x-ray diffractograms of the ferrite specimens exhibited wide peaks, indicating the extremely small crystallites in the samples. The structural parameters computed from the diffraction data, as shown in Table I, indicate that the size of ferrite samples lies in the nano-range.

Here, the lattice constant a was calculated as follows: $a = d * (h^2 + k^2 + l^2)^{1/2}$, where h, k, and l are the Miller indices of the planes with interplanar spacing d for the corresponding characteristic peaks. Meanwhile, the Debye–Scherrer formula was used to estimate the variation in the crystallite size, denoted by the letter D, as[27]

Crystallite Size, $D = k * \lambda / b * \cos q$.

The constant k is determined by the shape of the crystallite size and has a value of 0.89. β represents the full width at half maximum of the intensity (in arbitrary units) versus the 2θ profile. λ corresponds to the wavelength of the Cu-Kα radiation, which is equal to 1.5406 Å, θ represents the Bragg diffraction angle, and D represents the crystallite size. The average crystallite size is 13–15 nm for the ferrite nanoparticles. XRD density was calculated by the formula: Density = $8M/Na^3$, where M is the molecular weight of the sample and N is Avogadro's number. The x-ray density value of 5.25 was higher than the corresponding physical density. The hopping lengths of the A and B lattice sites of the spinel ferrite samples were also calculated using the lattice constant. Localized states are present at the band edges of polycrystalline solids, resulting from the absence of long-range orders. In these states, conduction can only occur through a hopping process facilitated by thermal energy.[28] The conductivity of solids is inversely related to the distance between hops and directly related to the rate at which electrons hop.[29]

The XRD pattern of ferrite polymer composites show a characteristic hump at 2θ around 25° which indicates the presence of the conducting polymers PANI and PPY in the composite samples. Also, with the polymerization, the peak intensity of the pristine samples has decreased.

The ferrite nanoparticles ($NiFe_2O_4$ and $CoFe_2O_4$) were subjected to Rietveld refinement analysis of their x-ray diffraction patterns. This analysis was performed using FULLPROF software, and the results are presented in Fig. 3. The Rietveld method, a widely recognized technique, is utilized to extract structural information from powder diffraction data. This method employs a least-squares procedure to compare the observed Bragg intensities with those calculated from a hypothetical structural model. The refined curves presented in Fig. 3 illustrate the intensity pattern observed in the experiment. The theoretically computed intensity based on the structural model is also depicted. The difference between these two intensities provides insight into the degree of refinement achieved by the model. The positions of the Bragg diffraction peaks are also indicated. Upon analysis of the refined x-ray diffraction (XRD) patterns, it is evident that the samples under investigation exist in a singular phase form. This observation suggests that the samples possess a uniform crystal structure throughout. Based on the chosen space group Fd-3m, the structural model was established with metal and iron atoms occupying the 8a and 16d spatial positions, respectively. The oxygen atom was positioned in the 32e spatial positions. The pseudo-Voigt profile function was used to describe the characteristics of the atoms. Table II presents the values of various refinement parameters for the ferrite samples, including the goodness of fit χ^2, Bragg R factor, lattice constant parameters, and density. It is evident that these values are in excellent concordance with the experimentally computed results.

Magnetic Measurements

Figure 5 displays the magnetization data for pure nickel and cobalt ferrites, namely the saturation magnetization (M_s) and coercivity (H_c). The measurements were taken at room temperature using a vibrating-sample magnetometer,

Table II Structural parameters computed from the refinement of the experimentally observed diffraction patterns

Sample	Lattice constant (Å)	Density (g/cm^3)	χ^2	Bragg R factor
$NiFe_2O_4$	8.3936	5.26	1.06	1.65
$CoFe_2O_4$	8.4331	5.29	1.26	1.96

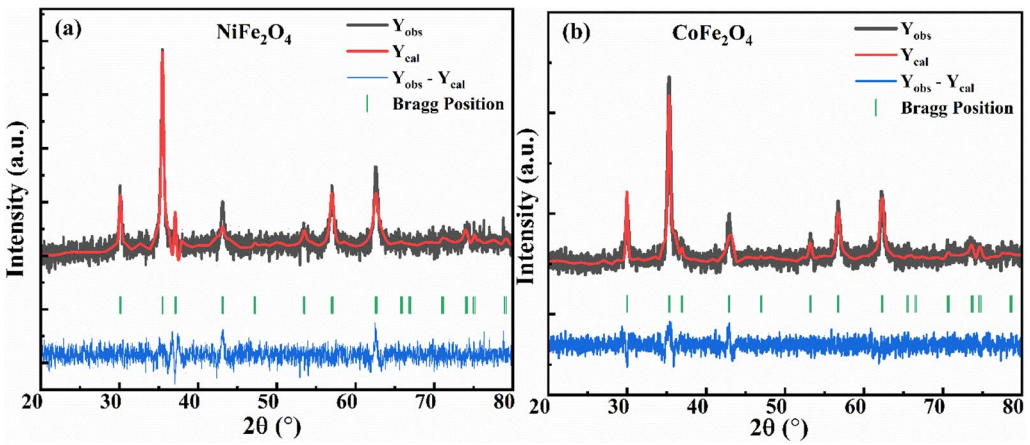

Fig. 3 Rietveld-refined patterns of the ferrite nanoparticles developed with the help of the structural model.

with a field range of ±1 T. The magnetic properties obtained from the hysteresis loop, namely coercivity (H_c), saturation magnetization (M_s), remanence magnetization (M_r), and squareness ratio ($R^2 = M_r/M_S$), are shown in Table II. In general, the samples of nickel ferrite and its composites exhibited characteristics of soft ferrite, while the cobalt ferrite and its hybrids exhibited characteristics of hard ferrite, characterized by high coercivity. All R^2 values lie within the range of 0.02–0.5, suggesting that the particles exist in a state of multiple randomly oriented domains.[30,31] The magnetic properties of the spinel ferrite lattice are mainly influenced by the A–B interactions, which result in the alignment of all magnetic spins at the A site in a particular direction and all those at the B site in the opposite direction, as shown in Fig. 4.[32]

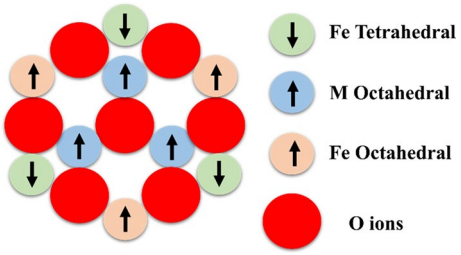

Fig. 4 Spin orientation at octahedral and tetrahedral sites of spinel ferrite samples.

The magnetic behaviour of nickel ferrite-based composites at room temperature is illustrated in Fig. 5b. The composite magnetization value is lower than that of pure ferrites, as illustrated in Table III.

This can be attributed to the presence of a non-magnetic medium composed of conducting polymer within the composite. The magnetic particles are isolated by the nonmagnetic conducting polymer, causing the collinear ferromagnetic arrangement of ferrites to be transformed into a non-collinear configuration.[33,34] The geometric and crystallographic characteristics of the ferrite nanoparticles are awry, as evidenced by their apertures, fissures, surface irregularity, and impurities. The process of depositing polymer on the ferrite surface and crystallite boundary results in the reduction of surface defects, including pores and cracks. This, in turn, causes a decline in the magnetic surface anisotropy of the ferrite particles. As a consequence, the coercivity of ferrite–PANI/PPY nanocomposites is lower than that of pure nano-ferrites.[35]

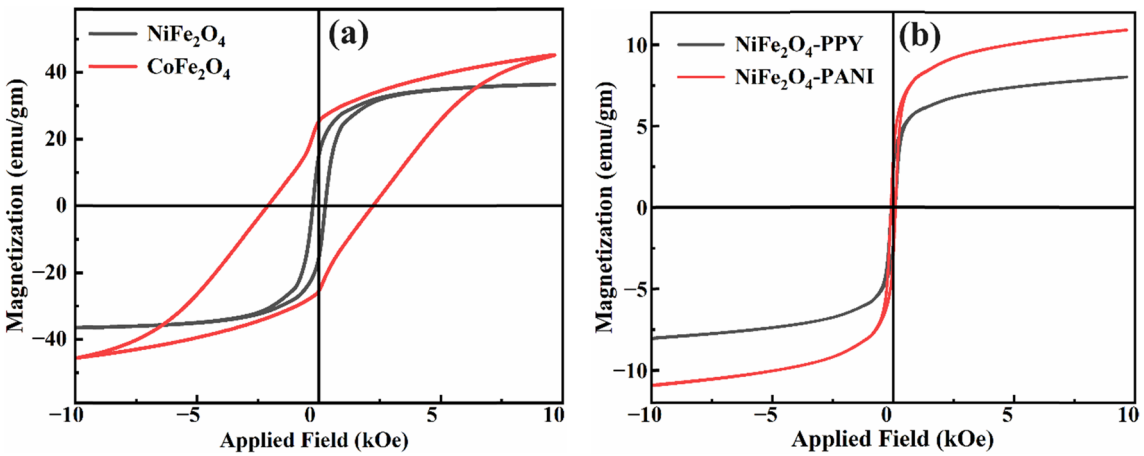

Fig. 5 Hysteresis loops of the ferrite and composites recorded at room temperature.

Table III Magnetic parameters of ferrites and their composites measured at room temperature

Sample	Saturation magnetization (emu/g)	Coercivity (Oe)	Remanent magnetization (emu/g)	Squareness ration
$NiFe_2O_4$	36.5	253	15.3	0.42
$NiFe_2O_4$–PPY	8.0	91	2.1	0.26
$NiFe_2O_4$–PANI	10.9	94	2.9	0.27
$CoFe_2O_4$	45.6	2216	25.4	0.56
$CoFe_2O_4$–PPY	12.1	782	3.1	0.26
$CoFe_2O_4$–PANI	15.3	796	3.8	0.25

Shielding Analysis

EMI shielding effectiveness refers to the capacity of materials to reduce the intensity of electromagnetic waves. It is quantified in decibels (dB) and is calculated as the logarithm of the incoming/incident intensity to the transmitted intensity of the electromagnetic wave across the shielding material. Electromagnetic waves typically undergo three distinct processes when they encounter a shielding material. A portion of the electromagnetic wave undergoes reflection upon interaction with charge carriers (e.g., electrons) on the material's surface; another portion is absorbed and dissipated as heat or a leaking current upon interaction with the material's electric or magnetic dipoles; and a final portion is multi-reflected within the shielding material due to the presence of interfaces or defect sites. Multi-reflected waves undergo the same heat dissipation or absorption as absorbed waves; therefore, absorption (A) and reflection (R) determine the overall EMI shielding effectiveness. The formula for the total EMI SE, as described above, is $SE_T = SE_R + SE_A$. The determination of shielding effectiveness (SE_R) and SE_A can be achieved by analysing the reflection, transmission, and absorption characteristics of the electromagnetic wave in interaction. The reflection coefficient (R), transmission coefficient (T), and absorption coefficient (A) were calculated by the S parameters (S_{11} or S_{22} and S_{21} or S_{12}) in a two-port network, according to the following equations[36]:

$$T = |S_{21}|^2 = |S_{12}|^2,\ R = |S_{11}|^2 = |S_{22}|^2 \text{ and } A = 1 - R - T.$$

Therefore, the shielding effectiveness due to various facets (SE_A, SE_R and SE_T) can be stated as

$$SE_R = -10\log(1-R) = -10\log\left(1-|S_{11}|^2\right),$$

$$SE_A = -10\log\left(1-A_{eff}\right) = -10\log\left(\frac{T}{(1-R)}\right) = 10\log\left(\frac{\left(1-|S_{11}|^2\right)}{|S_{21}|^2}\right),$$

$$SE_T = SE_R + SE_A = -10\log\left(|S_{21}|^2\right).$$

The current work examines shielding in the X-band frequency range of conducting polymers acting as a host matrix with a 1:1 ferrite absorber and 2.00-mm-thick materials. The SE fluctuation of the ferrite–PANI/PPY composites in the X-band (8–12.4 GHz) frequency range is shown in Fig. 6. It is widely recognized that pure PANI or pure ferrites have poor microwave attenuation qualities. With a value of 36 dB, the cobalt ferrite–PANI composites had the best shielding efficacy among all samples. This might be because cobalt ferrite has the highest magnetization, and absorption is also caused by magnetic dipoles.[37] The absorption losses are directly related to the permeability of the materials, so as the magnetic moment of the ferrite nanoparticles increases, the magnetic dipole losses also increase, resulting in higher absorption losses.

$$SE_A = 20d(\mu_r\omega\sigma)^{1/2}\log 10(e).$$

The overall shielding efficacy of the nickel ferrite–PANI composites is between 25 and 30 dB, which is much lower than that of cobalt ferrite composites, as nickel ferrite is a

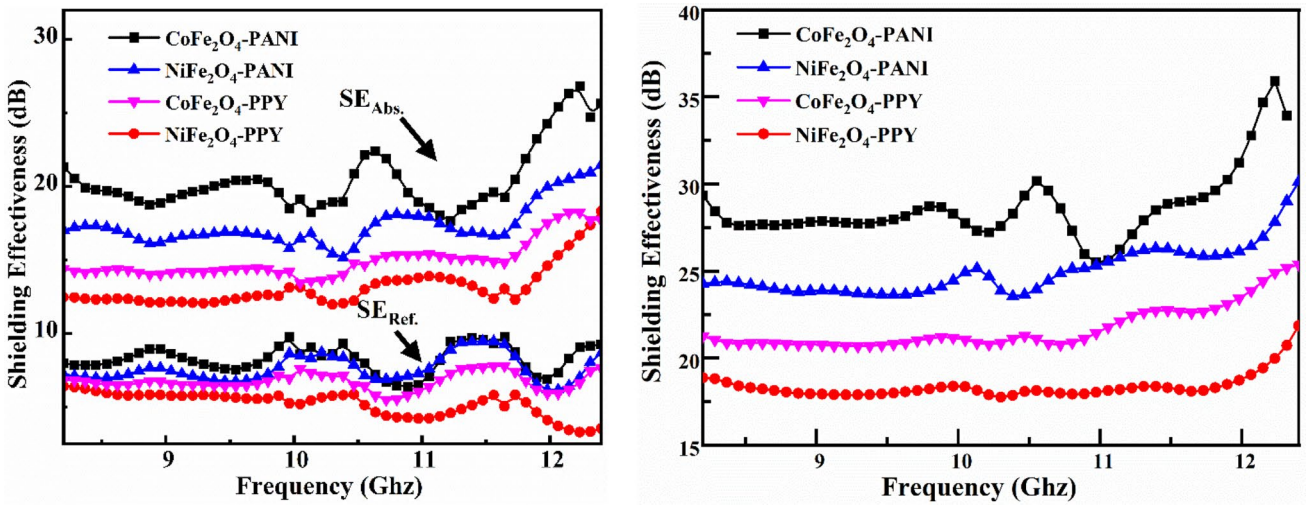

Fig. 6 Electromagnetic shielding effectiveness (due to reflection, absorption and total) of the composite samples in X-band frequency region.

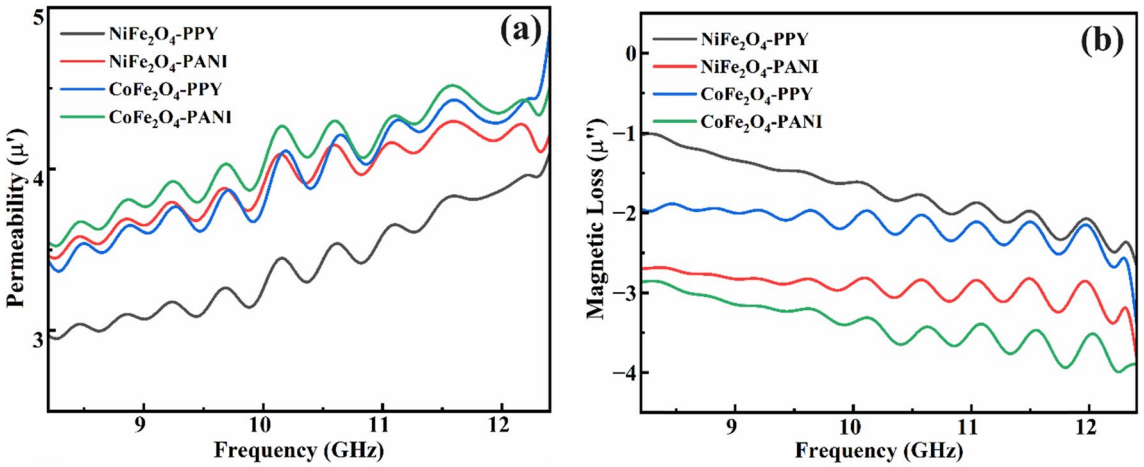

Fig. 7 Magnetic permeability and loss parameters of the composites recorded from vector network analyser measurements.

soft magnetic material with low magnetization. The cooperative effect is evident in the microwave properties of the absorber when ferrites, known for their high magnetic loss mechanism, are combined with PANI, which exhibits interfacial polarization and dipole relaxation. Many polymer-based filler hybrids face limitations such as low thermal conductivity, poor heat resistance, susceptibility to ageing, and relatively high thickness. These factors often limit their use in the smart and small-scale electronics industries. Thus, it is crucial to create polymer matrix composites that contain evenly distributed, highly absorptive fillers, which can form strong connections with the polymer. This is essential in order to achieve effective shielding. From Fig. 6a, it is clear that the shielding effectiveness is largely varied for the absorption behaviour while reflection attenuation is almost the same for all the composite samples. This shows the direct proportional effect of magnetic losses on the sustainable shielding response with almost constant effectiveness in the entire frequency range.

The relative complex permeability ($\mu_r = \mu' - j\mu''$) of the composites was calculated in order to determine the probable microwave absorption characteristics. This computation is shown in Fig. 7. Hysteresis loss, natural resonance, domain wall resonance, and the eddy current effect are some of the theoretical reasons proposed to explain the major role that magnetic losses play in microwave absorption.[38] On the microwave properties of the absorber, the synergistic impact of ferrites, which display a magnetic loss mechanism, and PANI/PPY, which assist an eddy current loss mechanism, is verified in Fig. 7.[39] Ferrites exhibit a loss mechanism that is characterized by magnetic loss. High levels of shielding efficiency were achieved by enhancing the interfacial dipolar polarization and scattering generated by the introduction of nano-sized ferrites into conducting polymers.[39] This resulted in high levels of shielding efficiency. The combination of these two factors results in a microwave absorber that is effective and lightweight, and has a wide bandwidth.

Conclusions

Nanoscale ferrite particles were synthesized using the sol–gel method at a low annealing temperature. Subsequently, their composites with PANI and PPY were formed through in situ polymerization. Cobalt and nickel ferrites exhibited favourable ferrimagnetic characteristics, as evidenced by their high saturation magnetization values. In contrast, nickel ferrite demonstrated lower coercivity, which can be attributed to its flexible nature. The electromagnetic interference (EMI) shielding characteristics of the composites have been the subject of extensive research in the X-band frequency range. The correlation between SE_A and magnetic parameters indicates that materials possessing high magnetization can yield superior absorption values. Throughout the entire X-band frequency range, the composites demonstrated exceptional shielding performance, with values of 20–30 dB for $NiFe_2O_4$–PANI/PPY and 25–36 dB for $CoFe_2O_4$–PANI/PPY. These values indicate that the composites are viable candidates for use as electromagnetic interference (EMI) shielding materials.

Acknowledgments The authors would like to express their gratitude to the Department of Physics at Gurugram University, as well as the Physics Department of Hindu College with the University of Delhi. We would like to express our gratitude to the University Science Instrumental Centre (USIC) for the characterization facilities.

Conflict of interest The authors declare that they have no conflict of interest.

References

1. L.H. Hemming, *Architectural Electromagnetic Shielding Handbook: A Design and Specification Guide* (Hoboken: Wiley, 2000).
2. E. Hanada, Y. Antoku, S. Tani, M. Kimura, A. Hasegawa, S. Urano, K. Ohe, M. Yamaki, and Y. Nose, *IEEE Trans. Electromagn. Compat.Electromagn. Compat.* 42, 470 (2000).
3. C.-K. Chou, *Int. J. Environ. Res. Public Health* 19, 16942 (2022).
4. W.R. Adey, *J. Cell. Biochem.Biochem.* 51, 410 (1993).
5. P. Sawai, P.P. Chattopadhaya, and S. Banerjee, *Mater. Today Proc.* 5, 9989 (2018).
6. A.K. Singh, A. Shishkin, T. Koppel, and N. Gupta, *Compos. Part B Eng.* 149, 188 (2018).
7. S. Geetha, K.K. SatheeshKumar, C.R.K. Rao, M. Vijayan, and D.C. Trivedi, *J. Appl. Polym. Sci.Polym. Sci.* 112, 2073 (2009).
8. J. Huang, *Adv. Polym. Technol.Polym. Technol.* 14, 137 (1995).
9. D. Trivedi and S. Dhawan, *Synth. Met.* 59, 267 (1993).
10. B. Reddy, Advances in Nanocomposites: Synthesis, Characterization and Industrial Applications (BoD--Books on Demand, 2011).
11. M.H. Al-Saleh and U. Sundararaj, *Carbon N. Y.* 47, 1738 (2009).
12. Z. Ding, S.Q. Shi, H. Zhang, and L. Cai, *Compos. Part B Eng.* 78, 266 (2015).
13. H. Tang, X. Jian, B. Wu, S. Liu, Z. Jiang, X. Chen, W. Lv, W. He, W. Tian, Y. Wei, Y. Gao, T. Chen, and G. Li, *Compos. Part B Eng.* 107, 51 (2016).
14. P. Didukh, J.M. Greneche, A. Ślawska-Waniewska, P.C. Fannin, and L. Casas, *J. Magn. Magn. Mater.Magn. Magn. Mater.* 242–245, 613 (2002).
15. S. Neveu, A. Bee, M. Robineau, and D. Talbot, *J. Colloid Interface Sci.* 255, 293 (2002).
16. R. Rahmayeni, Z. Zulhadjri, N. Jamarun, E. Emriadi, and S. Arief, *Orient. J. Chem.* 32, 1411 (2016).
17. T.H. Ting, R.P. Yu, and Y.N. Jau, *Mater. Chem. Phys.* 126, 364 (2011).
18. P. Los, A. Lukomska and R. Jeziorska, *Polimery* 61, 663 (2016).
19. S.H. Hosseini and A. Asadnia, *J. Nanomater.Nanomater.* 2012, 1 (2012).
20. Z.A. Boeva and V.G. Sergeyev, *Polym. Sci. Ser. C* 56, 144 (2014).
21. F. Kanwal, S.A. Siddiqi, A. Batool, M. Imran, W. Mushtaq, and T. Jamil, *Synth. Met.* 161, 335 (2011).
22. P. Yadoji, R. Peelamedu, D. Agrawal, and R. Roy, *Mater. Sci. Eng. B* 98, 269 (2003).
23. C.L. Yuan, Y.S. Hong, and C.H. Lin, *J. Magn. Magn. Mater. Magn. Magn. Mater.* 323, 1851 (2011).
24. A.H. Elsayed, M.S. MohyEldin, A.M. Elsyed, A.H. Abo Elazm, and E.M. Younes, *Int. J. Electrochem. Sci.* 6, 206 (2011).
25. L. Zhao, H. Yang, X. Zhao, L. Yu, Y. Cui, and S. Feng, *Mater. Lett.* 60, 1 (2006).
26. S. Bhukal, M. Dhiman, S. Bansal, M.K. Tripathi, and S. Singhal, *RSC Adv.* 6, 1360 (2016).
27. A. Manikandan, J. Judith Vijaya, M. Sundararajan, C. Meganathan, L.J. Kennedy, and M. Bououdina, *Superlattices Microstruct. Microstruct.* 64, 118 (2013).
28. U.V. Chhaya, B.S. Trivedi, and R.G. Kulkarni, *Phys. B Condens. Matter* 262, 5 (1999).
29. M.A. Gabal, R.M. El-Shishtawy, and Y.M. Al Angari, *J. Magn. Magn. Mater.Magn. Magn. Mater.* 324, 2258 (2012).
30. K.P. Thummer, M.C. Chhantbar, K.B. Modi, G.J. Baldha, and H.H. Joshi, *J. Magn. Magn. Mater.Magn. Magn. Mater.* 280, 23 (2004).
31. N.D. Chaudhari, R.C. Kambale, D.N. Bhosale, S.S. Suryavanshi, and S.R. Sawant, *J. Magn. Magn. Mater.Magn. Magn. Mater.* 322, 1999 (2010).
32. M.U. Rana, T. Abbas, and F. Khawaja, *Mater. Lett.* 52, 389 (2002).
33. T.T. Srinivasan, P. Ravindranathan, L.E. Cross, R. Roy, R.E. Newnham, S.G. Sankar, and K.C. Patil, *J. Appl. Phys.* 63, 3789 (1988).
34. N. Gupta, A. Verma, S.C. Kashyap, and D.C. Dube, *J. Magn. Magn. Mater.Magn. Magn. Mater.* 308, 137 (2007).
35. M. Ashokkumar, N.T. Narayanan, B.K. Gupta, A.L.M. Reddy, A.P. Singh, S.K. Dhawan, B. Chandrasekaran, D. Rawat, S. Talapatra, P.M. Ajayan, and P. Thanikaivelan, *ACS Sustain. Chem. Eng.* 1, 619 (2013).
36. A.P. Singh, S. Anoop Kumar, A. Chandra, and S.K. Dhawan, *AIP Adv.* 1, 022147 (2011).
37. B. Lu, X.L. Dong, H. Huang, X.F. Zhang, X.G. Zhu, J.P. Lei, and J.P. Sun, *J. Magn. Magn. Mater.Magn. Magn. Mater.* 320, 1106 (2008).
38. K. Singh, A. Ohlan, R.K. Kotnala, A.K. Bakhshi, and S.K. Dhawan, *Mater. Chem. Phys.* 112, 651 (2008).
39. Y.-Y. Kim, J.-M. Yun, Y.-S. Lee, and H.-I. Kim, *Carbon Lett.* 12, 48 (2011).